Characterization of Protein Dynamics in Asymmetric Cell Division by Scanning Fluorescence Correlation Spectroscopy

Zdeněk Petrášek,* Carsten Hoege,† Alireza Mashaghi,† Thomas Ohrt,* Anthony A. Hyman,† and Petra Schwille*

*Biophysics Group, Biotechnologisches Zentrum, Technische Universität Dresden, Dresden, Germany; and †Max Planck Institute of Molecular Cell Biology and Genetics, Dresden, Germany

ABSTRACT The development and differentiation of complex organisms from the single fertilized egg is regulated by a variety of processes that all rely on the distribution and interaction of proteins. Despite the tight regulation of these processes with respect to temporal and spatial protein localization, exact quantification of the underlying parameters, such as concentrations and distribution coefficients, has so far been problematic. Recent experiments suggest that fluorescence correlation spectroscopy on a single molecule level in living cells has great promise in revealing these parameters with high precision. The optically challenging situation in multicellular systems such as embryos can be ameliorated by two-photon excitation, where scattering background and cumulative photobleaching is limited. A more severe problem is posed by the large range of molecular mobilities observed at the same time, as standard FCS relies strongly on the presence of mobility-induced fluctuations. In this study, we overcame the limitations of standard FCS. We analyzed in vivo polarity protein PAR-2 from eggs of *Caenorhabditis elegans* by beam-scanning FCS in the cytosol and on the cortex of *C. elegans* before asymmetric cell division. The surprising result is that the distribution of PAR-2 is largely uncoupled from the movement of cytoskeletal components of the cortex. These results call for a more systematic future investigation of the different cortical elements, and show that the FCS technique can contribute to answering these questions, by providing a complementary approach that can reveal insights not obtainable by other techniques.

INTRODUCTION

Asymmetric division of early embryonic cells is essential for future cell diversity and is preceded by the establishment of cell polarity. A polarization signal leads to distinct concentrations of polarity factors in different cellular domains of the cell.

A good system for studies on polarization and asymmetric cell division is the one-cell *C. elegans* embryo (1–3). Here the first cell division is regulated by PAR proteins, among others (3–5), and requires the motility of the highly dynamic actomyosin cortex (contractions and flows) and the asymmetric localization of PAR proteins (6–8).

The polarization of the fertilized embryo is initiated by an interaction of the centrosome with the cortex (9) and leads to a cortical flow of actomyosin from the posterior toward the anterior part of the cell. This flow is closely connected with the accumulation of PAR-1 and PAR-2 at the posterior, and the restriction of PAR-3, PAR-6, and PKC-3 to the anterior half of the cell.

At a later maintenance phase, the asymmetric redistribution of the PAR proteins back to the whole cortex is prevented by their antagonistic interactions (10). Non-muscle myosin NMY-2, a component of the actomyosin cortex, is required through all phases, and after polarity establishment asymmetrically distributes with a more contractile cortex on the anterior side.

Binding of PAR-1 and PAR-2 to the cortex depends on a functional actomyosin cytoskeleton, as inhibition by cytochalasin B, an actin inhibitor, or downregulation of NMY-2 by RNAi inhibits binding. While direct interaction between PAR-2 and NMY-2 has not been demonstrated, PAR-1 can bind directly to NMY-2 in vivo, and PAR-1 localization is dependent on PAR-2 (7,8).

Although several polarity components of the *Caenorhabditis elegans* embryo have been discovered, it remains largely unclear how the asymmetry of the cortex-associated proteins before and during the first division is established and maintained, and how the proteins interact, move, and redistribute within the embryo on the molecular level.

The localization and redistribution of proteins involved in polarity is usually studied by fluorescence microscopy. While this imaging technique reveals the protein distribution and dynamics in living embryo on the second or subsecond timescale, its low temporal resolution does not allow the observation of fast dynamics on the scale of microseconds to milliseconds.

Here we apply standard fluorescence correlation spectroscopy (FCS) to measure the relatively fast diffusion of PAR-2, NMY-2, CDC-37, and a membrane-binding PH domain protein in cytosol. Circular scanning FCS (sFCS) is employed to investigate the considerably slower motion of the two cortex-associated proteins PAR-2 and NMY-2, a task practically impossible with standard FCS.

In FCS, the statistical analysis of the detected fluorescence signal by means of the autocorrelation function reveals important information about the dynamics of the diffusing

Submitted April 10, 2008, and accepted for publication August 26, 2008.

Zdeněk Petrášek and Carsten Hoege contributed equally to this work.

Address reprint requests to Petra Schwille, E-mail: petra.schwille@biotec.tu-dresden.de.

Editor: Alberto Diaspro.

0006-3495/08/12/5476/11 $2.00

doi: 10.1529/biophysj.108.135152

species, such as diffusion coefficients and the type of motion (11–13). Scanning FCS, a modification of the standard FCS with the measurement volume being scanned in a controlled fashion across the sample (14), has been introduced to overcome problems with low statistical accuracy in systems with slow diffusion (15,16), to minimize the effects of photobleaching of slowly diffusing molecules, or for other reasons (17–19).

We show that PAR-2 and non-muscle myosin NMY-2 diffuse freely in cytoplasm, with diffusion coefficients lower than expected in aqueous environment, most likely due to collisions with large components of the crowded cytoplasm, formation of larger complexes, or due to transient binding. On the cortex, both proteins exhibit highly dynamic nonuniform distribution. NMY-2 is localized in well-defined patches of the actomyosin cortex that changes its contractility throughout the cell cycle (6). Interestingly, PAR-2 assembles in a less discrete and more dynamic pattern than NMY-2. Scanning FCS autocorrelations of NMY-2 decay at a longer timescale with a sharp falloff, characteristic of directed motion. On contrary, PAR-2 motion is faster and the autocorrelation decay is more gradual, indicating multicomponent diffusive or even subdiffusive behavior.

The presented results show that FCS and sFCS are techniques suitable for the study of protein dynamics in an asymmetric dividing embryo on the temporal scales ranging from microseconds to seconds, and demonstrate that PAR-2 and NMY-2 show largely independent motion on the cortex.

MATERIALS AND METHODS

Experimental setup

The experiments were performed on a homebuilt two-photon laser scanning microscope (14,20) using an UPLAPO 60× W3/IR objective (Olympus, Hercules, CA). The excitation was provided by a tunable Ti:Sapphire laser (Mira 900-F, Coherent, Santa Clara, CA) with the wavelength set to 920 nm, and an average power of 5 mW. The laser beam is steered by two galvanometer scanners fully controllable by software, allowing the system to operate in two modes: a conventional imaging laser scanning microscope mode, and an sFCS mode, where the beam is scanned along a circular path with a user-defined radius and frequency. The fluorescence, collected by the objective and transmitted through an appropriate emission filter, is detected by an avalanche photodiode (model No. SPCM-CD2801, PerkinElmer, Wellesley, MA). For correlation measurements, the stream of detected photocounts is either directly autocorrelated with a multiple-tau hardware correlator (ALV-6000, ALV, Langen, Germany), or processed by the SPC-830 module (21) (Becker & Hickl, Berlin, Germany) to obtain timing of every photoncount with resolution 13.1 ns, and stored for further analysis.

The time of a point-FCS measurement at one location was 10×10 s. The time of one sFCS measurement was ~100 s, corresponding to 30,000 scan orbits at the used frequency of 300 Hz. The scan radii used in this work were in the range 2–9 μm, depending on the size of the flat part of the embryo cortex.

Biological system

C. elegans worms were cultured at 16°C on nematode growth media plates seeded with OP50 bacteria, and shifted to 25°C a day before imaging (22). GFP::PAR-2 (TH129) (23), GFP::PH-PLC1δ1 (24) and NMY-2::GFP (25) were described before. Briefly, GFP fusion proteins were expressed from stable transgenic worm lines from the pTH-GFP vector under the control of the pie-1 promoter. A transgenic worm line expressing GFP::CDC-37 from the pie-1 promoter (vector pTH-GFP-Gateway, containing the enhanced GFP variant) was produced by microparticle bombardment of unc-119(ed3) worms (26).

The fertilized eggs taken from adult worms were released by slicing animals open with a pair of needles in M9 buffer. Then the eggs were placed on agarose gel spread in a thin layer on a coverslip, and covered with another coverslip. The specimen was turned upside down and observed on an inverted microscope, as described above. The embryos were observed either with objective focus in the equatorial plane (cytoplasm FCS measurements), or with the focus near the coverslip, where the embryo was partially flattened and larger part of the embryo cortex was in focus, thus allowing sFCS measurements.

The sFCS measurements were performed in the maintenance phase after pseudocleavage and before the second cell division. During this time period, the cortex is relaxed after the myosin contractile foci have disassembled, and does not show strong contractile activity as observed in the polarity establishment phase (6). No measurements were performed during pseudocleavage and cytokinesis because of large-scale cortical movements (cell cortex rotation) accompanying cell division. However, more precise specification concerning the phase of the cell cycle was not made, due to the relatively long acquisition time needed (~100 s) and the comparatively short period without large-scale coordinated cortical movements (approximately minutes).

Data analysis

The fluorescence autocorrelation curves $g(\tau)$ obtained with the hardware correlator according to the definition

$$g(\tau) = \langle \delta F(t) \delta F(t+\tau) \rangle / \langle F(t) \rangle^2 \tag{1}$$

were analyzed using the model of free diffusion in three-dimensional space (12),

$$g(\tau) = \frac{g_0}{\left(1 + \frac{\tau}{\tau_D}\right)\sqrt{1 + \frac{\tau}{w^2 \tau_D}}}, \tag{2}$$

where $\langle F(t) \rangle$ is the average fluorescence intensity over the whole measurement, $\delta F(t) \equiv F(t) - \langle F(t) \rangle$, g_0 is the amplitude of the autocorrelation function, $\tau_D = a^2/D$ is the diffusion time, a is the $e^{-1/2}$ width of the measurement volume approximated by a Gaussian function ($a = 0.14$ μm in our case), w is the form factor describing the extension of the measurement volume in the axial direction, and D is the diffusion coefficient. The autocorrelation curves measured on the flattened part of the cell cortex were analyzed by an equivalent model for diffusion in two dimensions, which can be obtained from Eq. 2 by letting $w \to \infty$.

The stream of photocounts recorded during the sFCS measurements was stored and autocorrelated off-line. Since the relevant dynamics occurs on the timescales only 1–2 orders of magnitude shorter than the permissible time of the measurement, the correlation analysis is affected by poor statistical accuracy at long correlation times. For this reason, compensated normalization was chosen in the calculation of the correlations, as it has been shown to provide higher accuracy estimates of the correlations at long correlation times (27). The autocorrelation with compensated normalization is defined in the following way:

$$g(\tau_k) = \left(\langle F(t_i) F(t_{i+k}) \rangle_i - F_0 F_k \right) / F_k^2, \tag{3}$$

where

$$F_0 = \frac{1}{N-k} \sum_{i=0}^{N-1-k} F(t_i), \quad F_k = \frac{1}{N-k} \sum_{i=k}^{N-1} F(t_i). \tag{4}$$

Scanning the measurement volume introduces periodic oscillations into the autocorrelation curve persisting typically as long as the correlation has a nonzero value. To preserve this periodic pattern, the autocorrelation has to be calculated with sufficiently high resolution even at long correlation times. The common multiple-tau correlation technique does not have sufficient temporal resolution at larger lag times, causing the oscillations to average out. The scanning autocorrelation curves were therefore calculated with linearly spaced channels of constant width (1 μs or 10 μs). To achieve realistic computation times, the correlation was calculated via Fourier transform of the detected photoncount sequence $\mathcal{F}(F(t))$ using the following relationship:

$$G(\tau) = \int F(t)F(t+\tau)dt = \mathcal{F}^{-1}(|\mathcal{F}(F(t))|^2). \quad (5)$$

The details on the implementation of the calculation of linear autocorrelation of a long data stream using Fourier transform have been published elsewhere (28).

The long-scale fluorescence fluctuations caused by the global changes of the fluorescence pattern resulted in fluctuations in the tails of the sFCS autocorrelation functions. These fluctuations do not reflect the local dynamics of the fluorescence pattern (fluctuations at any given position along the scanned circle), and were therefore filtered out from the calculated curves by the following procedure. The fluctuating fluorescence signal $F(t)$ was assumed to consist of the local fluctuating signal $f(t)$ modulated by a slowly changing global modulation function $h(t)$: $F(t) = f(t)h(t)$. The function $h(t)$ was estimated from the measured fluorescence $F(t)$ by smoothing $F(t)$ with a bin width of 0.13 s, which corresponds to 39 scan periods. It follows from the above-mentioned definition that the autocorrelation $g_F(t)$ of $F(t)$ is related to the autocorrelation $g_f(\tau)$ of $f(t)$ and the autocorrelation $g_h(\tau)$ of $h(t)$ in the following way:

$$g_F(\tau) + 1 = (g_f(\tau) + 1)(g_h(\tau) + 1). \quad (6)$$

The desired autocorrelation $g_f(\tau)$ was then calculated from Eq. 6 using known $g_F(\tau)$ and $g_h(\tau)$. Since the effective number of measurement locations along the circle is large, this procedure does not affect the resulting temporal autocorrelation profile, as would be the case in a measurement with fixed detection volume. This filtering procedure is demonstrated in Fig. S3 in Supplementary Material, Data S1.

Similarly, average nonuniformity of fluorescence along the scanned circle can produce additional oscillations in the autocorrelation curve, reflecting this nonuniformity. Again, these fluctuations can be filtered out applying Eq. 6, where $h(t)$ is now the average fluorescence intensity along the scanned circle over the whole measurement, and $g_h(\tau)$ is the autocorrelation of $h(t)$ (see Fig. S3 in Data S1). The effect of this procedure is similar to the phase-normalized autocorrelation introduced by Skinner et al. (18) to separate fluctuations due to immobilized particles.

Free diffusion on a two-dimensional surface while scanning the beam with frequency ω in a circle of radius R leads to the following model autocorrelation (16):

$$g(\tau) = \frac{g_0}{1+\frac{\tau}{\tau_D}} e^{-\frac{R^2\sin^2(\omega\tau/2)}{a^2(1+\tau/\tau_D)}}. \quad (7)$$

The preexponential term corresponds to the standard autocorrelation of diffusion process in two dimensions, and the exponential factor describes the periodic modulation due to the scanning motion. The scanning autocorrelation consists of peaks located at correlation times equal to the integer multiples of the scan period T, that is, at times when the scanning focus returns to the initial position. The peak maxima coincide with the autocorrelation value that would be obtained in the absence of scanning (the preexponential term in Eq. 7). When the scan radius R is much larger than the size of the measurement volume a, the correlation between the peaks is practically zero, since the fluorescence at points located far from each other (far compared to a) is generally uncorrelated. The width of the peaks forming the autocorrelation increases with the correlation time, as the molecules diffuse further and further away from their initial position (see Fig. S2 in Data S1). When the molecular motion is much slower than the scanning speed, the shape of the peaks in the autocorrelation function is largely determined by the exponential factor in Eq. 7. Therefore, the exponential factor with an effective width parameter $a'^2 = a^2(1 + \tau/\tau_D)/R^2$ and an amplitude A as two fitting parameters were used to fit the peaks of the experimental sFCS autocorrelation functions.

The scanning autocorrelation can be viewed as a part of the full spatiotemporal correlation $g(x, \tau)$; that is, the correlation of fluorescence between two locations spaced by the distance x at two time points delayed by the time τ. This becomes apparent when one realizes that only the values at integral multiples of the scan period are autocorrelations at the same location, while the values at all other times are actually spatial cross correlations between two locations at a distance x:

$$x = 2R\sin(\omega\tau/2). \quad (8)$$

This equation relates the correlation time τ to the spatial correlation coordinate x, or alternatively, to the phase φ of the circular motion: $\varphi = \omega\tau$. Scanning FCS samples the full spatiotemporal correlation at coordinates (x, τ) linked by Eq. 8. This sampling is fine enough when the scanning motion is much faster than the relevant timescales determined by the investigated molecular motion. The sFCS autocorrelation can then be displayed as a two-dimensional plot with the axes formed by the x and τ coordinates, and the correlation value color-coded.

The spatiotemporal correlation $g(x, \tau)$ contains more information than a temporal correlation $g(\tau)$, and possibility to measure it experimentally gives a better chance to distinguish between different models of transport. For example, the spatiotemporal correlation of diffusion in two dimensions

$$g(x,\tau) = \frac{g_0}{1+\frac{\tau}{\tau_D}} e^{-\frac{x^2}{4a^2(1+\tau/\tau_D)}} \quad (9)$$

exhibits broadening in space with longer correlation times as the molecules diffuse from their initial position. On the other hand, binding to/detachment form a surface,

$$g(x,\tau) = g_0 e^{-k\tau} e^{-\frac{x^2}{4a^2}}, \quad (10)$$

does not show any spatial broadening, since the molecules do not move laterally and disappear fast after detachment from the surface. Although these two models already show different dependence of the autocorrelation $g(\tau)$ on the correlation time, the additional differences in spatial correlation, accessible experimentally with sFCS, can help to better discriminate between alternative models (see Fig. S1 in Data S1 for several models of spatiotemporal correlation).

RESULTS

Diffusion in cytoplasm

The PAR-2 and NMY-2 proteins are known to localize in cytoplasm and in different parts of the embryo cortex, depending on the phase of the cell cycle (29). Whereas PAR-2 localizes almost exclusively on the posterior cortex after polarity establishment, NMY-2 localizes predominantly on the anterior cortex, while being less contractile on the posterior (Fig. 1, *A* and *B*). However, posterior localization of PAR-2 depends on NMY-2 (7). Therefore, an interesting question is whether PAR-2 can bind to the cortex directly by association with NMY-2. We tested this hypothesis by studying the dynamics of both proteins in the cytosol and on the cortex by FCS.

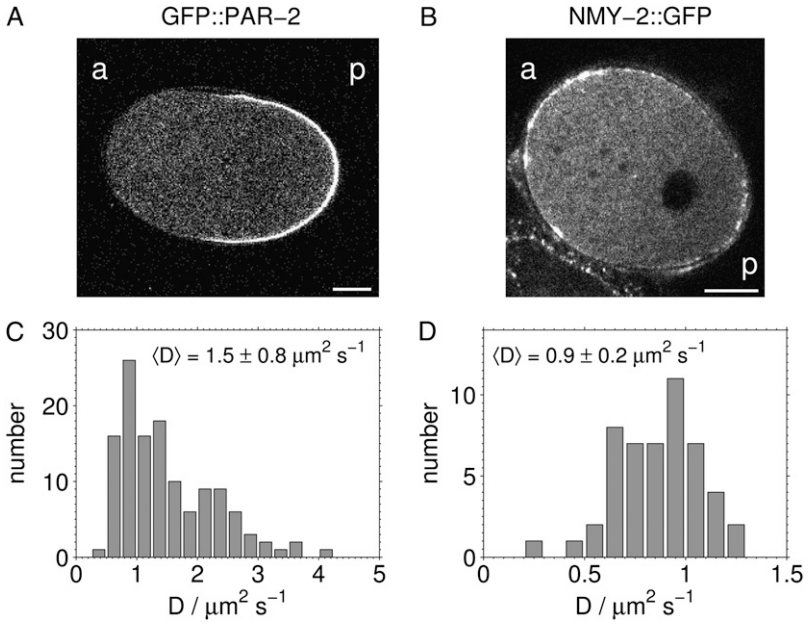

FIGURE 1 Diffusion coefficients of GFP::PAR-2 (*A* and *C*) and NMY-2::GFP (*B* and *D*) in the cytosol. The measurement volume was positioned into different parts of the cytosol, while focused into the midplane of the embryo (*A* and *B*), and the measured autocorrelation curves were fitted to Eq. 2. The distributions of the obtained diffusion coefficients *D* are shown in panels *C* (GFP::PAR-2) and *D* (NMY-2::GFP). (Scale bar, 10 μm. *a*, anterior; *p*, posterior.)

We have employed two-photon FCS with the measurement volume positioned in a fixed location within the cytoplasm to measure the mobility of GFP::PAR-2 and NMY-2::GFP. The measurement volume was positioned away from the pronuclei; the movement of the pronuclei did not influence the measured protein dynamics because it occurs on a much longer timescale. The autocorrelation curves were analyzed using the model of diffusion in three dimensions (Eq. 2). The distributions of the obtained diffusion coefficients are shown in Fig. 1 *C* (GFP::PAR-2) and Fig. 1 *D* (NMY-2::GFP). The mean values of the diffusion coefficients determined from the measured distributions are shown in Table 1, with the errors indicating the widths of the distributions. The differences in the distributions of the diffusion coefficients of the two proteins indicate that PAR-2 and NMY-2 in the cytosol do not diffuse as a part of a common complex. The possibility to use Eq. 2 to describe the measured autocorrelations indicates predominantly diffusive behavior of the two proteins in cytoplasm.

For comparison, we performed analogous FCS measurements on two other proteins in cytosol: GFP::CDC-37 and GFP::PH. CDC-37, a protein of similar size to PAR-2 (Table 1), is required for polarity establishment and mutual exclusion of anterior and posterior PAR proteins (30). It is uniformly distributed in both anterior and posterior halves of the embryo and does not localize on the cortex. The PH domain, a small protein domain derived from mammalian PLC1δ1, is known to bind to PIP_2 lipid present in the plasma membrane, and therefore serves as a membrane marker (24,31). Embryos expressing GFP::PH display very bright fluorescence on the plasma membrane and weaker fluorescence in the cytosol, permitting standard FCS measurements in both. The measured diffusion coefficients of both proteins again exhibit broadened distributions. The mean values together with the standard deviations indicating the distribution widths are shown in Table 1.

In addition to cytosolic diffusion, it was possible to measure standard FCS autocorrelations of the GFP::PH on the membrane, by focusing onto the flattened bottom part of the embryo as described below, and thus preventing the movement of the membrane out of focus. The diffusion of the GFP::PH on the membrane is ~1 order-of-magnitude slower than in the cytosol (Table 1). The relatively fast diffusion of all the investigated proteins in cytosol and the PH domain on the membrane (compared to PAR-2 and NMY-2 dynamics on the cortex; see below) means that no distortions due to photobleaching occur.

TABLE 1 Diffusion coefficients determined with FCS

Protein	Location	M/kDa	D/μm^2 s^{-1}
NMY-2	Cytosol	257	0.9 ± 0.2
PAR-2	Cytosol	96	1.5 ± 0.8
CDC-37	Cytosol	69	4.8 ± 1.3
PH	Cytosol	47	8.1 ± 2.0
PH	Membrane	47	1.1 ± 0.3

The error indicates the width of the distribution of *D*. The molecular mass *M* is inclusive the GFP label.

Scanning FCS on the cortex

Attempts to perform standard FCS measurements on PAR-2 and NMY-2 localized on the cortex by positioning the measurement volume on the cortex when focused in the embryo midplane (Fig. 1, *A* and *B*) did not provide satisfactory results. The main reason was the motion of the embryo caused by its development, on the timescale of ~100 s needed for the

measurement. Motion of the cortex as a whole out of the measurement volume cannot be separated from the slow motion of molecules within the cortex, thereby compromising the results.

Another problem with measurements with fixed volume is the low statistical accuracy due to the very slow motion of the molecules on the cortex: during the maximum realistic measurement time, limited by the development of the embryo, insufficient number of molecules passes through the measurement volume, resulting in low accuracy of the averaging procedure. Additionally, photobleaching can occur during the long residence time in the measurement volume.

To overcome these problems, we have used circle sFCS, where the measurement volume is moved along a circular path with a known radius and frequency (16,18). The objective was focused near the coverslip onto the flattened bottom part of the embryo. In this way, the largest possible part of the cortex was simultaneously present in focus. The radius was chosen as large as possible so that the whole scanning path lied within the focused part of the cortex (Fig. 2, *A* and *B*). Longer scan path means that information from effectively more independent volumes is averaged, implying better statistical accuracy. The data obtained in this way represents an average over the scanned path, and it is therefore implicitly assumed that the typical dynamics are the same at all probed locations.

The fluorescence intensity trace was recorded with the SPC-830 module and its autocorrelation was calculated offline as described in Materials and Methods. Typical autocorrelation curves of GFP::PAR-2 and NMY-2::GFP are shown in Fig. 3, *A* and *B*, respectively. The peaks on the blue curves at times nT, where T is the scan period $T = 1/300$ s, correspond to the autocorrelation at the same location after n rotations of the measurement volume. The shapes of the peaks (not discernible in the figure) were fitted to the model as expressed by Eq. 7, and the fitted amplitude of every peak is marked as a black dot in the plots in Fig. 3, *A* and *B*. An example of fits to several selected peaks of a GFP::PAR-2 autocorrelation function is shown in Fig. S2 in Data S1. The curve formed by the amplitudes of all peaks then represents the loss of correlation of the fluorescence pattern on the cortex, and reflects the temporal redistribution of this pattern, in a similar way as an ordinary FCS curve reflects the passage of molecules through the measurement volume.

The typical decay of autocorrelation of GFP::PAR-2 was found to differ from that of NMY-2::GFP, as shown in Fig. 4, where several normalized autocorrelation curves (formed by peak maxima as described above) of each protein are plotted. The autocorrelation of GFP::PAR-2 decays over a broad temporal range and cannot be described by simple diffusion with one component (see Fig. 5). Its extended shape suggests multicomponent or anomalous diffusion. The autocorrelation decay of NMY-2::GFP is steeper than the autocorrelation of a two-dimensional diffusional process, possibly indicating contribution of translational motion, which alone leads to a steep $\exp(-(\tau/\tau_f)^2)$ temporal dependence (32). The motion of NMY-2::GFP on the cortex is slower than GFP::PAR-2, as can be seen by comparison of the curves in Fig. 4. Surprisingly, the dynamics of NMY-2::GFP as characterized by the autocorrelation curves was found to be similar in both anterior and posterior parts of the cell, independently of the higher fluorescence intensity in the anterior part.

The distribution of both the proteins on the cortex was nonuniform, with rapidly changing pattern (Fig. 2, *A* and *B*). The sizes of the features in both cases were near or below the

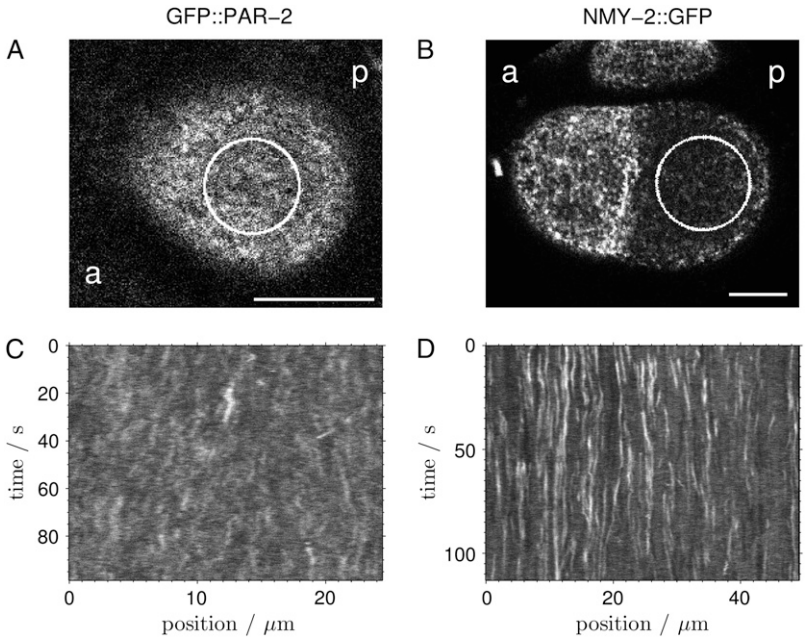

FIGURE 2 Nonuniform fluorescence pattern of GFP::PAR-2 (*A* and *C*) and NMY-2::GFP (*B* and *D*) on the cortex. The objective was focused near the coverslip onto the flattened part of the embryo. The circles in panels *A* and *B* indicate the scan path for sFCS measurements. (*C* and *D*) The fluctuating fluorescence intensity recorded in the sFCS measurement is displayed in a two-dimensional plot, where the horizontal axis corresponds to one revolution (scan period T), and the vertical axis to subsequent revolutions during the course of measurement (from *top* to *bottom*). The columns in the plot then show the fluorescence fluctuations at individual positions along the scanned circle. (*C*) GFP::PAR-2, D: NMY-2::GFP. (Scale bar, 10 μm. *a*, anterior; *p*, posterior.)

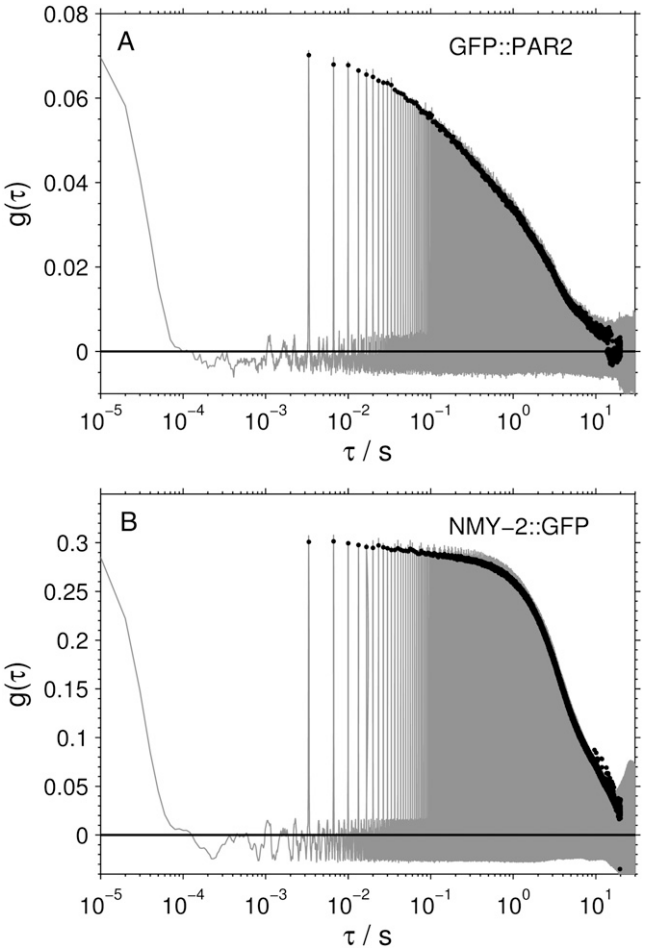

FIGURE 3 The experimental fluorescence autocorrelations from sFCS measurements (*shaded*). The amplitudes of the peaks obtained from fits to Eq. 7 are indicated by solid dots. (*A*) GFP::PAR-2, (*B*) NMY-2::GFP.

optical resolution. The autocorrelation curves describe also the motion and the dynamics of this pattern rather than only the dynamics of individual independently moving molecules. The pattern of NMY-2::GFP consists of bright spots with size comparable to or below the resolution limit (6), whose movement appears to be to some extent coordinated and partially directional (nondiffusive). This can be seen in Fig. 2 *D*, where the fluorescence intensity from sFCS measurements is plotted in a two-dimensional plot in such a way that each line corresponds to one revolution, the horizontal axis corresponds to points along the circle, and the measurement time increases from the top to the bottom. The inclined vertical traces originate from bright spots crossing the scanned circle at a certain angle. Parallel traces belong to spots moving in the same direction and indicate therefore coordinated motion. The fluorescence distribution of GFP::PAR-2 on the cortex is also found to be nonhomogeneous and highly dynamic. However, it appears to be much less concentrated into discrete spots and its motion is less coordinated (Fig. 2 *C*).

The character of motion of fluorescently labeled molecules is reflected by spatiotemporal correlation $g(\tau, x)$. Therefore,

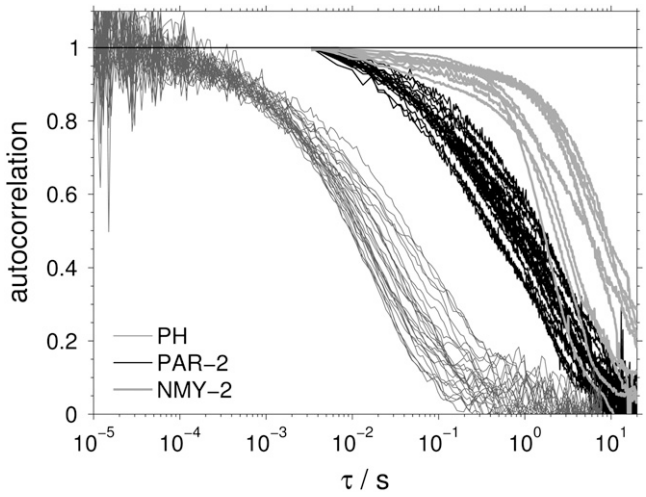

FIGURE 4 Comparison of sFCS autocorrelations of GFP::PAR-2 (*black*) and NMY-2::GFP (*thick gray*) on the cortex and FCS autocorrelations of GFP::PH (*thin gray*) on the membrane from measurements in several embryos. The sFCS autocorrelations are formed by the fitted amplitudes of the peaks as shown in Fig. 3.

the sFCS correlation data were displayed as functions of the correlation coordinates (τ, x), as described in Materials and Methods (Figs. 6 and 7). Both PAR-2 and NMY-2 exhibit spatial broadening of the correlations with increasing correlation time τ, as can be better seen in Figs. 6 *B* and 7 *B*, where the correlations are normalized at every time τ to a maximum. The broadening appears at shorter times in case of PAR-2

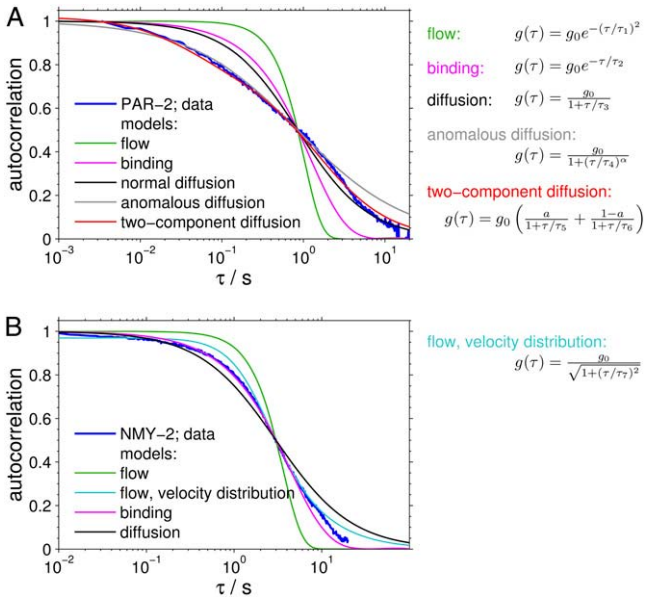

FIGURE 5 Comparison of a typical sFCS autocorrelation (*blue*) of GFP::PAR-2 (*A*) and NMY-2::GFP (*B*) with several simple models of transport: uniform flow (*green*), binding/dissociation (*magenta*), normal diffusion (*black*), anomalous diffusion (*gray*), normal two-component diffusion (*red*), and flow with a Gaussian distribution of speeds, centered at $v = 0 : p(v) \sim \exp(-v^2/(2\sigma_v^2))$ (*cyan*). The parameters τ_i are the characteristic time constants of the relevant process.

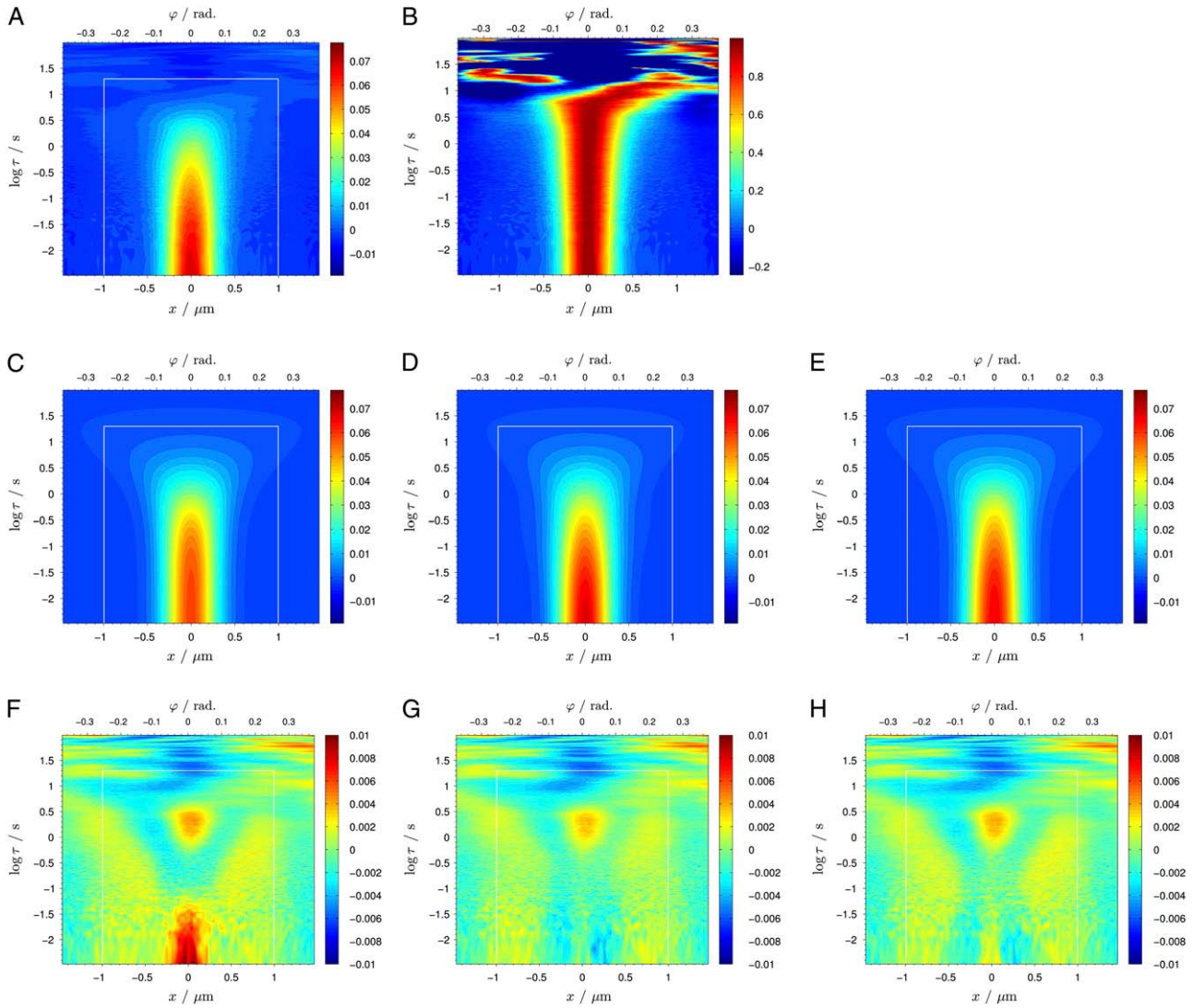

FIGURE 6 sFCS autocorrelation of GFP::PAR-2 displayed in spatiotemporal representation, and fits to three different models. The value x is the spatial and τ the temporal correlation coordinate. (*A*) The spatiotemporal autocorrelation. (*B*) The spatiotemporal autocorrelation normalized to the maximum at each τ value to emphasize the spatial broadening. (*C* and *F*) Fit to a one-component diffusion model and the residuals of the fit ($\chi^2 = 4.61 \times 10^{-6}$). The white rectangle denotes the fitting range. (*D* and *G*) Fit to a two-component diffusion model and the fit residuals ($\chi^2 = 3.99 \times 10^{-6}$). (*E* and *H*) Fit to a model with one diffusion and one binding/dissociation components, and the fit residuals ($\chi^2 = 4.37 \times 10^{-6}$). The correlation coordinate x (corresponding to the distance along the scanned circle) can be equivalently expressed by the scan phase φ, or by the time from the peak maximum τ. These three coordinates are related to each other in the following way: $x = 2R \sin(\omega\tau/2)$, $\varphi = \omega\tau$.

than NMY-2, which is consistent with the shorter correlation times, implying faster motion. The normalized correlations also show that the time $\tau \sim 10$ s represents a practical accuracy limit in these measurements, beyond which the data are dominated by noise. The PAR-2 correlation was fitted to three models: one-component diffusion, two-component diffusion, and one-component diffusion with one binding/dissociation component, using an appropriate linear combination of Eqs. 9 and 10 (Fig. 6, *C–H*). As expected from observations made above (Fig. 4), the one-component diffusion model does not describe the data well. Out of the two models with two components, two-component diffusion leads to a better fit with the data than one diffusion and one binding component, as judged by the residual plots and the values of χ^2 (Fig. 6, *G* and *H*). No fitting of NMY-2 spatiotemporal correlation was attempted, because the spatial features start to appear at correlation times too close to the accuracy limit (Fig. 7 *B*).

DISCUSSION

Scanning FCS on the cortex

The presented results of the sFCS measurements demonstrate that this technique is capable of capturing the dynamics, which is too slow for conventional FCS. By scanning along a

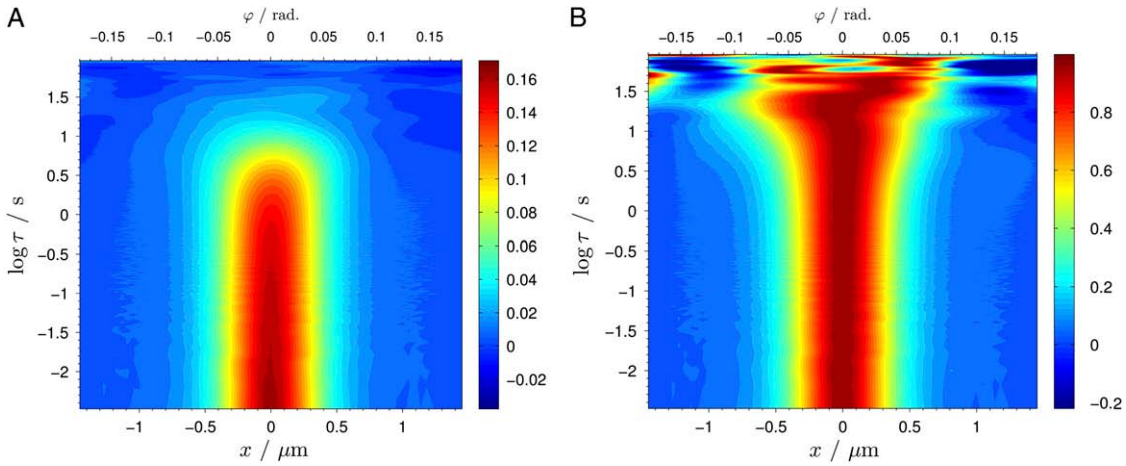

FIGURE 7 sFCS autocorrelation of NMY-2::GFP displayed in spatiotemporal representation. (*A*) The spatiotemporal autocorrelation. (*B*) The spatiotemporal autocorrelation normalized to the maximum at each τ.

circle, multiple locations are probed pseudo-simultaneously, and sufficient averaging can be achieved in a time shorter by one-to-two orders of magnitude than the time necessary for a measurement with a fixed detection volume. Furthermore, no photobleaching of slowly moving molecules was observed (Fig. 2, *C* and *D*), which can be attributed to the fact that each location along the circular path is illuminated for only a small fraction of the scan period *T*.

The sFCS correlations represent information averaged along the scanned circle. To see whether there are any statistically significant variations in dynamics at different points, we divided the raw data and calculated autocorrelations at individual locations along the circle (see Fig. S4 in Data S1). The individual curves are strongly affected by poor statistics (which is one of the reasons for averaging over a larger area); however, within the limits of this accuracy, the dynamics are comparable at all points along the circle.

The comparison of the sFCS autocorrelation curves (Fig. 4) of GFP::PAR-2 and NMY-2::GFP shows that the dynamics of both proteins on the cortex are clearly distinct from each other. While the motion of GFP::PAR-2 is faster and has a rather diffusive or subdiffusive character, the motion of NMY-2::GFP is slower and the sharp falloff of the autocorrelation indicates contribution of directed flow. Fig. 5 *B* shows by comparison with several models that the NMY-2::GFP autocorrelation decay is steeper than that of diffusion, but more gradual than flow with uniform speed. A reasonable assumption of distribution of flow velocities results in an autocorrelation curve with a slope close to the experimental data, as demonstrated on the example of Gaussian velocity distribution $p(v)\sim\exp(-v^2/(2\sigma_v^2))$. Although the binding model matches the data well, the observed lateral motion of myosin clusters is not compatible with this model.

The partially coordinated flow of myosin might be related to the deformation of the actin cortex to which the bright spots of NMY-2::GFP are thought to be linked. The different falloff times of the NMY-2::GFP autocorrelation curves are likely to be caused by natural variations in cortical motion in any given experiment. The cortical flow speed during polarity establishment has been previously determined as ~4 μm min^{-1} (5) with maximum value of 7.7 μm min^{-1} (6), which translates into equivalent flow times τ_f of the correlation curves of 4.1 s or 2.1 s, respectively. This value is comparable to the characteristic decay times of the NMY-2 sFCS autocorrelations (Fig. 4), suggesting that the myosin moves with similar velocities at both polarity establishment and maintenance phases. During the polarity establishment phase the myosin patches move all in the same direction, resulting in a net cortex flow, while in the later phases the motion is directionally uncorrelated, preventing appearance of any large-scale flows, and being observable only as a reorganization of the punctuate fluorescence pattern.

The decay of the sFCS autocorrelation of PAR-2 is more gradual than the loss of autocorrelation due to the following simple transport processes: uniform flow, binding/dissociation, and normal diffusion, as shown in Fig. 5 *A*. Combination of binding with diffusion or flow cannot result in an autocorrelation that is flatter than in any of these processes alone. The PAR-2 autocorrelation decay can be better described by the model of anomalous diffusion with a time-stretching parameter α. Even better match with the experimental data can be achieved by considering contribution of two (or more) motion components, each with its own type of transport and time constant, as demonstrated by two-component diffusion in Fig. 5 *A*. The fits to the spatiotemporal correlation (Fig. 6) also favor a two-component diffusion model over a model with one-component diffusion and one binding/dissociation component. The multicomponent diffusion model is consistent with the presence of slow bright clusters (Fig. 2 *C*) and faster smaller complexes or individual molecules. The gradual autocorrelation decay, broadening of sFCS autocorrelation peaks with increasing lag time, and the dynamics of bright patches as seen in Fig. 2 *C* all suggest presence of diffusional motion within the cortex. This does not, however, exclude the

possibility of minor contribution of binding kinetics to one or more components of motion, with diffusion still being the dominant transport mechanism.

The differences in the dynamics between PAR-2 and NMY-2 proteins inferred from the autocorrelation data show that although there might be minor fractions that bind each other, the proteins move within the cortex mostly independently.

The faster motion of PAR-2 relative to that of NMY-2, which is assumed to reflect the cortex dynamics, and the presence of a clearly detectable pattern (Fig. 2 *A*), raises the question of the role of the membrane present above the cortex in the localization of PAR-2. Although the dynamics of PAR-2 on the cortex are slower than those of the PH domain on the membrane, the localization of PAR-2 with components of the membrane cannot be excluded. The existence of a PAR-2 pattern implies reduced molecular mobility, and the autocorrelations measured with sFCS are likely to be dominated by the dynamics of the bright PAR-2 pattern rather than the dynamics of individually diffusing PAR-2 molecules, therefore leading to a slower-decaying autocorrelation. It is not clear whether the bright pattern dynamics represents motion of bright clusters containing many GFP-labeled PAR-2 molecules, or whether the observed dynamics is a net effect of simultaneous growth and disassembly of otherwise static clusters (or combination of the two phenomena). Developing a model of fluorescence autocorrelation and spatiotemporal correlation resulting from the latter mechanism might help to discriminate between the two processes.

The measured mean diffusion coefficient of the PH domain on the membrane (1.1 $\mu m^2\ s^{-1}$) is comparable with that of fluorescent lipid analogs in plasma membranes of rat basophilic leukemia cells (0.8–0.9 $\mu m^2\ s^{-1}$) and human embryonic kidney cells (1.4 $\mu m^2\ s^{-1}$) (33), suggesting free diffusion of GFP::PH bound to PIP_2 in the membrane.

Cheeks et al. (5) used fluorescence recovery after photobleaching (FRAP) to show that photobleached PAR-2 on cortex completely recovers on the scale of tens of seconds. Their FRAP results are limited by the time resolution of 2 s, and do not permit further characterization of the type of the recovery process. With scanning FCS, we could access shorter timescales down to the millisecond range, and identify the presence of more components of motion. The two-component diffusion can be furthermore linked to the observed heterogeneous highly dynamic PAR-2 cortex pattern, not reported previously. Scanning FCS has the advantage of higher temporal resolution over FRAP, thus forming a bridge between the FRAP technique applicable on the timescales of seconds and longer, and a standard FCS operating at millisecond scales and shorter. Representing the sFCS data in terms of spatiotemporal correlation further increases the information obtainable with sFCS.

Other fluorescence correlation techniques could in principle be applied to study the dynamics of the cortex-localized proteins. For example, spatiotemporal image correlation spectroscopy has been used to produce a map of flows from a sequence of images (34). Our preliminary results with spatiotemporal image correlation revealed limitations on the spatial and temporal resolution imposed by the high transport speeds and the available fluorescence signal in our data (28). Scanning FCS currently appears to be the optimal approach for the studied problem on the way between point- and image-correlation techniques.

Another technique for studying dynamics is particle tracking, which, however, requires identification of the features to be tracked. While this may be successful for NMY-2, it would be hardly possible for PAR-2 with our data, where the brighter fluorescent areas cannot be unambiguously identified and separated from their surroundings in subsequent image frames due to low contrast and imaging rate and high noise. This is likely to be the case also for some other PAR proteins. To reliably compare dynamics of two or more proteins, it would be, however, preferable that the data are obtained using the same technique. We see a possible alternative to tracking in a certain combination of tracking and correlation techniques, where the image features need not be identified, but their displacement from one image frame to another is determined by correlation, in a way similar to image registration techniques commonly used, for example, in medical imaging. The feasibility of this approach applied to a comparatively noisy fluorescence microscopy images remains to be tested.

Diffusion in cytoplasm

The dynamics of the investigated GFP-labeled proteins in the cytosol can be reasonably well described by free diffusion. The observed spread of diffusion times is mainly due to the presence of long-time fluctuations in the fluorescence intensity, which affect the autocorrelation curves at long times and limit the accuracy of the fits to the simple diffusion model. The measured diffusion coefficients therefore reflect the fastest component of the motion of the proteins in the cytoplasm.

Although the solvent viscosity of cytoplasm, as measured by rotational mobility (i.e., microviscosity), is known to be similar to that of water, the translational diffusion of probes of various sizes indicates considerably higher and additionally size-dependent apparent viscosity. This effect has been explained by heterogeneity and crowding of the cytoplasm, where collisions with large structures and reversible binding lead to effectively lower diffusion coefficient and stronger dependence of the diffusion coefficient on the particle size, than that predicted by the Stokes-Einstein relationship (35,36).

The measured diffusion coefficients of the investigated proteins in cytosol are all significantly smaller than the diffusion coefficient of free GFP in buffer (87 $\mu m^2\ s^{-1}$) (37): the fastest GFP::PH is $\sim 11\times$ slower, and the slowest NMY-2::GFP $\sim 100\times$ slower. Purified GFP-labeled proteins were not available to perform direct comparison with their diffusion in a buffer. The simplifying assumption of a cube

root dependence of the diffusion coefficient on the molecular mass predicts only 1.5–2× smaller diffusion coefficient of the individual protein molecules in buffer compared to GFP. These results indicate the role of cytoplasmatic crowding on the motion of the investigated proteins.

Although PAR-2 and CDC-37 are of similar size, PAR-2 diffusion is approximately three times slower, indicating possible localization in a larger complex or self-association. Similarly, the low diffusion coefficient of NMY-2 may be a consequence of association with other cytoplasmic components and homodimerization. The possible involvement of PAR-2 and NMY-2 in large protein complexes could be linked to the mechanism by which they become localized to the cortex.

CONCLUSION

We have shown that FCS and sFCS can be used to study the dynamics of fluorescently labeled molecules on both short and long timescales even in such a complex and dynamic system as a polarized embryo that will divide asymmetrically, by overcoming the limitations of low statistical accuracy and photobleaching. Although cortex localization of PAR-2 depends on the presence of NMY-2 (8), our data indicate that PAR-2 is not recruited to the cortex by binding to posterior localized NMY-2 patches. By using circular sFCS, we could show that PAR-2 dynamics are faster than NMY-2, and further that PAR-2 distribution in the cortex is not uniform but heterogeneous, with a highly dynamic pattern distinct from that of NMY-2. It is therefore more likely that NMY-2 changes the properties of the cortex in a way that PAR-2 can associate with it, and presence of PAR-2 on the cortex might be inhibitory for NMY-2 contractility.

Circular sFCS, with its single-molecule sensitivity and full utilization of the fluorescence signal, provides information about the molecular dynamics and the type of motion, which is too slow for standard FCS, and not resolvable with imaging. Furthermore, sFCS provides information on spatial correlation in addition to temporal correlation, facilitating better characterization of transport processes in living organisms and discrimination between different models on basis of their spatiotemporal correlation.

Measurement along a perimeter of a relatively large circle overcomes two significant limitations encountered in FCS when applied to slowly moving molecules: photobleaching accompanied by depletion of fluorescent molecules in the fixed measurement area, and statistical noise due to the insufficient number of molecules crossing the measurement volume during the measurement. In comparison to imaging, higher temporal resolution, determined by the scanning frequency, is achieved with sFCS. Furthermore, by using two-photon excitation one additionally benefits from the possibility of long measurement times without disturbing the embryo development.

Future sFCS studies on other polarity proteins, along with fluorescence microscopy and RNAi experiments, will contribute to a better understanding of asymmetric cell division in *C. elegans* and in other systems.

SUPPLEMENTARY MATERIAL

To view all of the supplemental files associated with this article, visit www.biophysj.org.

We thank Carrie Cowan and Nathan Goehring for stimulating discussions.

C.H. was supported by an Ernst Schering Foundation Postdoctoral fellowship. Funding was provided by The International Human Frontier Science Program grant No. RGP 5-2005, and Europäische Fond für Regionale Entwicklung project No. 4212-06-02.

REFERENCES

1. Cowan, C. R., and A. A. Hyman. 2004. Asymmetric cell division in *C. elegans*: cortical polarity and spindle positioning. *Annu. Rev. Cell Dev. Biol.* 20:427–453.
2. Schneider, S. Q., and B. Bowerman. 2003. Cell polarity and the cytoskeleton in the *Caenorhabditis elegans* zygote. *Annu. Rev. Genet.* 37:221–249.
3. Nance, J. 2005. PAR proteins and the establishment of cell polarity during *C. elegans* development. *Bioessays.* 27:126–135.
4. Munro, E. M. 2006. PAR proteins and the cytoskeleton: a marriage of equals. *Curr. Opin. Cell Biol.* 18:86–94.
5. Cheeks, R. J., J. C. Canman, W. N. Gabriel, N. Meyer, S. Strome, and B. Goldstein. 2004. *C. elegans* PAR proteins function by mobilizing and stabilizing asymmetrically localized protein complexes. *Curr. Biol.* 14:851–862.
6. Munro, E., J. Nance, and J. R. Priess. 2004. Cortical flows powered by asymmetrical contraction transport PAR proteins to establish and maintain anterior-posterior polarity in the early *C. elegans* embryo. *Dev. Cell.* 7:413–424.
7. Guo, S., and K. J. Kemphues. 1996. A non-muscle myosin required for embryonic polarity in *Caenorhabditis elegans*. *Nature.* 382:455–458.
8. Boyd, L., S. Guo, D. Levitan, D. T. Stinchcomb, and K. J. Kemphues. 1996. PAR-2 is asymmetrically distributed and promotes association of P granules and PAR-1 with the cortex in *C. elegans* embryos. *Development.* 122:3075–3084.
9. Cowan, C. R., and A. A. Hyman. 2004. Centrosomes direct cell polarity independently of microtubule assembly in *C. elegans* embryos. *Nature.* 431:92–96.
10. Cuenca, A. A., A. Schetter, D. Aceto, K. Kemphues, and G. Seydoux. 2003. Polarization of the *C. elegans* zygote proceeds via distinct establishment and maintenance phases. *Development.* 130:1255–1265.
11. Rigler, R., and E. S. Elson, editors. 2001. Fluorescence Correlation Spectroscopy, 1st Ed. Theory and Application, Chemical Physics Series. Springer Verlag, Berlin.
12. Bacia, K., and P. Schwille. 2003. A dynamic view of cellular processes by in vivo fluorescence auto- and cross-correlation spectroscopy. *Methods.* 29:74–85.
13. Petrov, E. P., and P. Schwille. 2008. Standardization and Quality Assurance in Fluorescence Measurements II: Bioanalytical and Biomedical Applications, Vol. 6, Springer Series on Fluorescence. Springer, Berlin, Heidelberg, New York.
14. Petrášek, Z., and P. Schwille. 2008. Single Molecules and Nanotechnology, Vol. 12, Springer Series in Biophysics. Springer, Berlin, Heidelberg, New York.
15. Petersen, N. O. 1986. Scanning fluorescence correlation spectroscopy. 1. Theory and simulation of aggregation measurements. *Biophys. J.* 49:809–815.

16. Berland, K. M., P. T. C. So, Y. Chen, W. W. Mantulin, and E. Gratton. 1996. Scanning two-photon fluctuation correlation spectroscopy: particle counting measurements for detection of molecular aggregation. *Biophys. J.* 71:410–420.

17. Amediek, A., E. Haustein, D. Scherfeld, and P. Schwille. 2002. Scanning dual-color cross-correlation analysis for dynamic co-localization studies of immobile molecules. *Single Mol.* 3:201–210.

18. Skinner, J. P., Y. Chen, and J. D. Müller. 2005. Position-sensitive scanning fluorescence correlation spectroscopy. *Biophys. J.* 89:1288–1301.

19. Digman, M. A., C. M. Brown, P. Sengupta, P. W. Wiseman, A. R. Horwitz, and E. Gratton. 2005. Measuring fast dynamics in solutions and cells with a laser scanning microscope. *Biophys. J.* 89:1317–1327.

20. Petrášek, Z., M. Krishnan, I. Mönch, and P. Schwille. 2007. Simultaneous two-photon fluorescence correlation spectroscopy and lifetime imaging of dye molecules in submicrometer fluidic structures. *Microsc. Res. Tech.* 70:459–466.

21. Becker, W., A. Bergmann, E. Haustein, Z. Petrášek, P. Schwille, C. Biskup, L. Kelbauskas, K. Benndorf, N. Klöcker, T. Anhut, I. Riemann, and K. König. 2006. Fluorescence lifetime images and correlation spectra obtained by multidimensional time-correlated single photon counting. *Microsc. Res. Tech.* 69:186–195.

22. Brenner, S. 1974. Genetics of *Caenorhabditis elegans*. *Genetics*. 77: 71–94.

23. Schonegg, S., A. T. Constantinescu, C. Hoege, and A. A. Hyman. 2007. The ρGTPase-activating proteins RGA-3 and RGA-4 are required to set the initial size of PAR domains in *Caenorhabditis elegans* one-cell embryos. *Proc. Natl. Acad. Sci. USA.* 104:14976–14981.

24. Audhya, A., F. Hyndman, I. X. McLeod, A. S. Maddox, J. R. Yates, A. Desai, and K. Oegema. 2005. A complex containing the Sm protein CAR-1 and the RNA helicase CGH-1 is required for embryonic cytokinesis in *Caenorhabditis elegans*. *J. Cell Biol.* 171:267–279.

25. Nance, J., E. M. Munro, and J. R. Priess. 2003. *C. elegans* PAR-3 and PAR-6 are required for apicobasal asymmetries associated with cell adhesion and gastrulation. *Development.* 130:5339–5350.

26. Praitis, V., E. Casey, D. Collar, and J. Austin. 2001. Creation of low-copy integrated transgenic lines in *Caenorhabditis elegans*. *Genetics*. 157:1217–1226.

27. Kojro, Z. 1991. Normalization and statistical noise level in the normalized autocorrelation function. Compensated normalization. *J. Phys. Math. Gen.* 24:L225–L229.

28. Petrášek, Z., C. Hoege, A. A. Hyman, and P. Schwille. 2008. Two-photon fluorescence imaging and correlation analysis applied to protein dynamics in *C. elegans* embryo. *Proc. SPIE.* 6860:68601L.

29. Cowan, C. R., and A. A. Hyman. 2007. Acto-myosin reorganization and PAR polarity in *C. elegans*. *Development*. 134:1035–1043.

30. Beers, M., and K. Kemphues. 2006. Depletion of the co-chaperone CDC-37 reveals two modes of PAR-6 cortical association in *C. elegans* embryos. *Development.* 133:3745–3754.

31. Hurley, J. H., and T. Meyer. 2001. Subcellular targeting by membrane lipids. *Curr. Opin. Cell Biol.* 13:146–152.

32. Palmer, A. G., and N. L. Thompson. 1987. Theory of sample translation in fluorescence correlation spectroscopy. *Biophys. J.* 51:339–343.

33. Bacia, K., D. Scherfeld, N. Kahya, and P. Schwille. 2004. Fluorescence correlation spectroscopy relates rafts in model and native membranes. *Biophys. J.* 87:1034–1043.

34. Brown, C. M., B. Hebert, D. L. Kolin, J. Zareno, L. Whitmore, A. R. Horwitz, and P. W. Wiseman. 2006. Probing the integrin-actin linkage using high-resolution protein velocity mapping. *J. Cell Sci.* 119:5204–5214.

35. Luby-Phelps, K. 2000. Cytoarchitecture and physical properties of cytoplasm: volume, viscosity. diffusion, intracellular surface area. *Int. Rev. Cytol.* 192:189–221.

36. Verkman, A. S. 2002. Solute and macromolecule diffusion in cellular aqueous compartments. *Trends Biochem. Sci.* 27:27–33.

37. Swaminathan, R., C. P. Hoang, and A. S. Verkman. 1997. Photobleaching recovery and anisotropy decay of green fluorescent protein GFP-S65T in solution and cells: cytoplasmic viscosity probed by green fluorescent protein translational and rotational diffusion. *Biophys. J.* 72:1900–1907.